Journal of the Mechanics and Physics of Solids 124 (2019) 634–642

Contents lists available at ScienceDirect

Journal of the Mechanics and Physics of Solids

journal homepage: www.elsevier.com/locate/jmps

Origin of serrated flow in bulk metallic glasses

Xie Xie[a,1], Yu-Chieh Lo[b,1], Yang Tong[c], Junwei Qiao[d], Gongyao Wang[a], Shigenobu Ogata[e,f,*], Hairong Qi[g], Karin A. Dahmen[h], Yanfei Gao[a,*], Peter K. Liaw[a,*]

[a] Department of Materials Science and Engineering, University of Tennessee, Knoxville, TN 37996, USA
[b] Department of Materials Science and Engineering, National Chiao Tung University, Hsinchu, 30010, Taiwan
[c] Materials Science and Technology Division, Oak Ridge National Laboratory, Oak Ridge, TN 37831, USA
[d] College of Materials Science and Engineering, Taiyuan University of Technology, Taiyuan 030024, China
[e] Department of Mechanical Science and Bioengineering, Graduate School of Engineering Science, Osaka University, Osaka 560-8531, Japan
[f] Center for Elements Strategy Initiative for Structural Materials (ESISM), Kyoto University, Kyoto 606-8501, Japan
[g] Department of Electrical Engineering and Computer Science, University of Tennessee, Knoxville, TN 37996, USA
[h] Department of Physics, University of Illinois at Urbana-Champaign, Urbana, IL 61801, USA

ARTICLE INFO

Article history:
Received 15 August 2018
Revised 9 November 2018
Accepted 24 November 2018
Available online 27 November 2018

Keywords:
Bulk metallic glasses
Thermoplasticity
Serrated flow
Kinetic Monte–Carlo

ABSTRACT

Bulk metallic glasses (BMGs) possess amorphous structure and show unique mechanical properties, such as extremely high strength and excellent damage tolerance, entitling them as potential structural materials. So far a great amount of work has been conducted to study BMGs' macroscopic mechanical properties and examine corresponding microscopic deformation defects. However, the connection between macroscopic inhomogeneous deformation at room temperature and microscopic deformation carriers is still poorly understood, due to the lack of an appropriate experimental technique to directly probe the inhomogeneous deformation process on the proper spatial and temporal scales. Here we present the deformation details via in situ thermal imaging about the evolution of heat bands associated with successive serration behavior. For the first time, our experimental work clarifies the coupling of serrated flows with shear band activities, especially the often omitted fine serrations induced by shear band nucleation or the early stage of propagation. Meanwhile, serration behavior of BMGs is simulated through the kinetic Monte Carlo (kMC) method by integrating local heating (thermal softening and β-relaxation) effects, which exhibits good agreement with experimental results. These findings will advance our fundamental understanding of the shear band operation down to microscopic level, which may shed light on the control of shear banding for the application of BMGs.

1. Introduction

Bulk metallic glasses (BMGs) deform inhomogeneously at room temperature through strongly localized shear banding observed in most deformation modes (e.g., compression, bending) (Greer, 1995; Ashby and Greer, 2006; Johnson, 1999; Wang et al., 2004; Greer et al., 2013). Thus, the investigation and characterization of shear band nucleation and propagation

* Corresponding authors.
E-mail addresses: ogata@me.es.osaka-u.ac.jp (S. Ogata), ygao7@utk.edu (Y. Gao), pliaw@utk.edu (P.K. Liaw).
[1] These two authors contributed equally to this work.

https://doi.org/10.1016/j.jmps.2018.11.015
0022-5096/

become essential to understand their deformation mechanism. As widely accepted, the nucleation of shear band in BMGs is heterogeneous because of inevitable structural heterogeneities, which was demonstrated by the facts that flow stress replaces ideal yielding stress (2∼3 times higher than flow stress (Tian et al., 2012; Egami et al., 2013)) for BMGs, whereas ideal elastic limit is approached by nanoscale mechanical testing due to "the smaller, the stronger" effect (Kumar et al., 2011; Wang et al., 2012). Following the heterogeneous nucleation, a mature shear band starts to form in the so-called propagation stage, but the propagation mechanism is still under debate due to the lack of direct observation. In general, two models have been proposed for the shear band propagation (Greer et al., 2013; Wright et al., 2009; Klaumunzer et al., 2011). Progressive shear model describes that the shear band initiates at one stress concentrator on one side of sample surface and propagates to the other side to form a shear plane (Greer et al., 2013; Wright et al., 2009; Klaumunzer et al., 2011; Ketov and Louzguine-Luzgin, 2013; Cao et al., 2009); the other one, the simultaneous shear model, illustrates that the shear occurs simultaneously across the sample to form a shear plane (Greer et al., 2013; Wright et al., 2009; Klaumunzer et al., 2011; Song and Nieh, 2011). Local heating at nucleation site observed by infrared (IR) camera supports the progressive shear model whereas simultaneous shear model is also evidenced by two smooth regions at two ends of the fracture surface. Recent thermograph work suggests that simultaneous model can be validated by the experimental results (Thurnheer et al., 2016), but notched sample used in this study may neglect the activities in the initiation stage. Simulation studies, however, suggested a two-stage scenario: a progressive shear front propagates to form a rejuvenated shear plane across the whole sample, and then the shear plane slides in a synchronized fashion.

To address the above debates and confusions, there is a pressing need for the direct observation of shear band initiation, propagation, and sliding. However, due to the extraordinary requirements of spatial and temporal resolution (generally tens of nanometers and several nanoseconds), very limited experimental techniques could be applied to the in situ study of shear band initiation and propagation. Among these methods, representative ones include acoustic emission (Klaumunzer et al., 2011) and high speed camera (Song and Nieh, 2011; Wright et al., 2013). The former has high sensitivity for temporal resolution, but it loses the capability of characterizing the spatial information of shear bands. The latter can successfully capture the shear offset during shear band operation, but miss the important information about shear band development at the early propagation stage without obvious shear offset. Besides the above two characterization methods, recent work has unveiled that temperature rises significantly within shear bands (Leamy et al., 1972; Wright et al., 2001; Lewandowski and Greer, 2006). To estimate the quantity of the heat release from shear bands, the fusible coating (Ketov and Louzguine-Luzgin, 2013; Lewandowski and Greer, 2006; Zhang et al., 2007; Slaughter et al., 2014) and thermograph (Thurnheer et al., 2016; Yang et al., 2006; Wang et al., 2012; Jiang et al., 2008) methods were utilized. The temperature was estimated as several thousands of Kelvin at shear band nucleation but decays dramatically due to heat conduction. By assuming the shear band as a planer heat source with zero thickness, both methods suggest a heat content of 0.4 – 2.2 kJ/m^2 released for Vit 1 ($Zr_{41.25}Ti_{13.75}Ni_{10}Cu_{12.5}Be_{22.5}$, atomic percent) in the shear band initialization. Variations of these values should be expected using different strain rates and sample geometries. Followed by extensive work, it becomes clearer that the local heating is not a driving factor for the shear localization but a consequence (Ketov and Louzguine-Luzgin, 2013; Lewandowski and Greer, 2006; Zhang et al., 2007; Gao et al., 2007). The question then arises: what is the role of the heat during the deformation for BMGs?

To tackle this question, a thermal imaging technique combined with a modified kMC simulation was developed in the present work. The infrared technique is capable of identifying the heat conduction associated with shear band operation, and establishing the important correlation of shear band kinetics with the serration behavior that always exhibited in BMGs' stress-strain curve. Through the image analysis of heat release and heat conduction recorded during the deformation of a Zr-based BMG, we revealed a sequential process for its inhomogeneous deformation: random fertile nucleation sites were activated at the beginning, then their growth in size and percolation led to the formation of a primary shear band, and a steady state of this mature shear band sliding was finally reached before fracture. The synchronized correlation of shear band activities with stress drops was observed and, meanwhile, the longstanding argument for the relatively small stress drop around yielding and in the steady state was clarified. Based on the heat activities from above experimental results, we developed the modified kMC model, which, as to our knowledge, firstly simulates the shear banding and serration of BMG. The results show that despite the limited resolution from the IR camera, the shear band activities could be inferred from the history of heat conduction, which yields an unprecedented understanding for the serration behavior in BMGs with the assistance of simulations.

2. Experimental procedures

The Zr-based BMG Vitreloy 105 (Vit-105, $Zr_{52.5}Cu_{17.9}Ni_{14.6}Al_{10.0}Ti_{5.0}$ in atomic percent, at.%) was used, according to its relatively good glass-forming ability and ductility. The samples were prepared by arc-melting the mixtures of constituent metals with purity higher than 99.9% volume percent in a Ti-gettered high-purity argon atmosphere, and the molten alloy is suction cast to a rod with a length of 60 mm. To prepare for the compression experiments, the rods were cut into cylindrical specimens with 4 mm in length and 2 mm in diameter. Two compression ends were carefully polished to be parallel.

The compression experiment was conducted by the Material Test System (MTS) 810 machine controlled by a computer at room temperature. The initial strain rate was set to 2×10^{-3}/s, and a data acquisition rate of 100 Hz was used for the analysis. During the compression process, a FLIR SC5000 Infrared (IR) Imaging System was employed to observe the dynamic evolution of temperature on the surface of the specimens at a frame rate of 300 Hz. This camera operates in the 2.5 to 5.1 μm

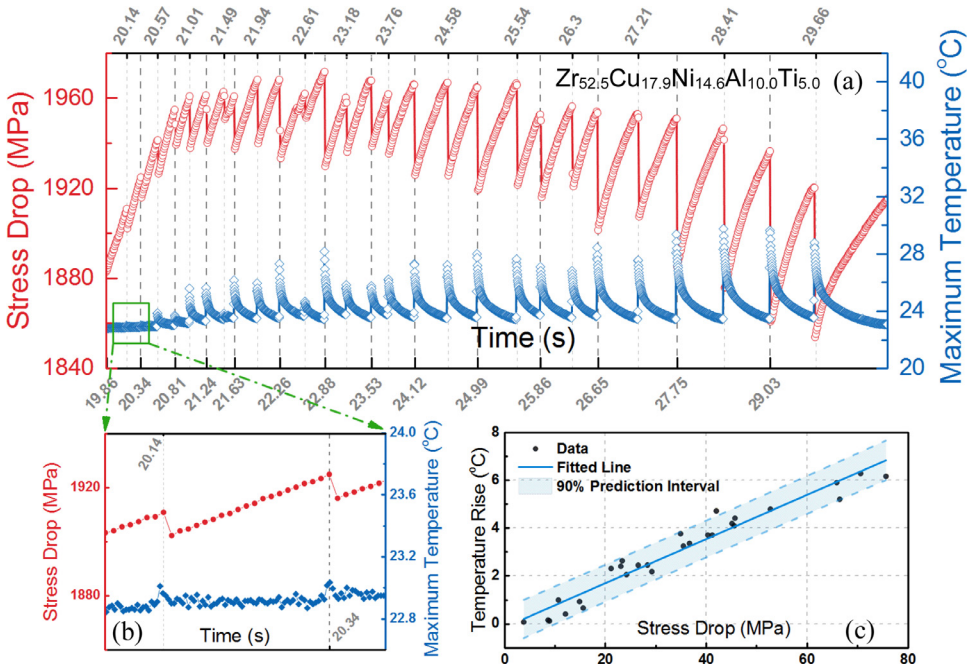

Fig. 1. (a) The corresponding time for the occurrence of stress drop and maximum temperature for each frame, (b) the magnified region of the early stage in (a) indicated by the green rectangular, and (c) the linear relationship between temperature rise and stress drop. (For interpretation of the references to colour in this figure legend, the reader is referred to the web version of this article.)

waveband, and is equipped with a cooled Indium Antimonide (InSb) detector with sensitivity smaller than 20 mK at room temperature. The spatial resolution of this camera can reach 15 μm. Before the experiment, a thermocouple was attached to a specimen to calibrate the IR camera. Each frame of the recorded video and temperature data were then analyzed.

3. Results

The temperature evolution on the sample surface from the 1st serration to the fracture was shown in Fig. 1 and Fig. S2 (supplementary document) recorded by an IR camera. A total of 27 serration events (not including fracture) can be identified by the heat bands. The histogram at the upper right corner shows the temperature distribution for each frame. At the beginning of the video, the heat activation can be found from both ends. Intuitively, each serration exhibits as a hot band on the surface, and its temperature and width generally become larger as the external load increases. Generally, the process of each serration event could be described as follows in the context of the heat band evolution (see each serration event in Figure S2 of the supplementary file). At the starting point of each stress drop, temperature burst can be found on the sample surface as a thin heat band (discontinued at an early stage), implying the initiation of the sudden slip. During the stress drop, the released amount of heat increases, leading to a dramatic temperature rise. When the stress drop reaches the bottom, which roughly marks the end of the heat releasing process, the heat band becomes wider due to heat dissipation. In the subsequent stress-rise region, no heat burst can be observed, and instead the heat continues being conducted to the surrounding low temperature region, resulting in significant diminish of surface temperature even before the next serration event.

It is evident that the occurrences of heat release coincide with the stress drop for each serration. To be more specific, in Fig. 1(a), the stress drop and the temperature burst are found to be correlated and synchronized with each other, demonstrating that the serration behavior is associated with thermal activities. The magnitudes of temperature rise and stress drop are calculated, and plotted in Fig. 1(c). A very good linear relationship can be found between these two quantities. In addition, small spots of temperature burst synchronizing with a small stress drop were also detected in Fig. 1(b), and will be discussed later.

To check the spatial correlation of the shear banding path for each serration, the first frame of each serration was superimposed. As illustrated in Fig. 2(a), the ridge-like morphology obviously reveals that most paths are located at the same position (at microscale) on the sample surface. Meanwhile, there exists temperature bursts at places other than the main ridge (marked as "immature shear band" in Fig. 2), which corresponds to the initiation of new shear bands for the 2nd, 4th, 7th, and 14th serration events. Figure S2 also indicates that after the 5th serration, a primary shear band path is formed. Subsequent serrations occur along this softened path, clearly suggesting a reactivation process of the shear band instead of new nucleation.

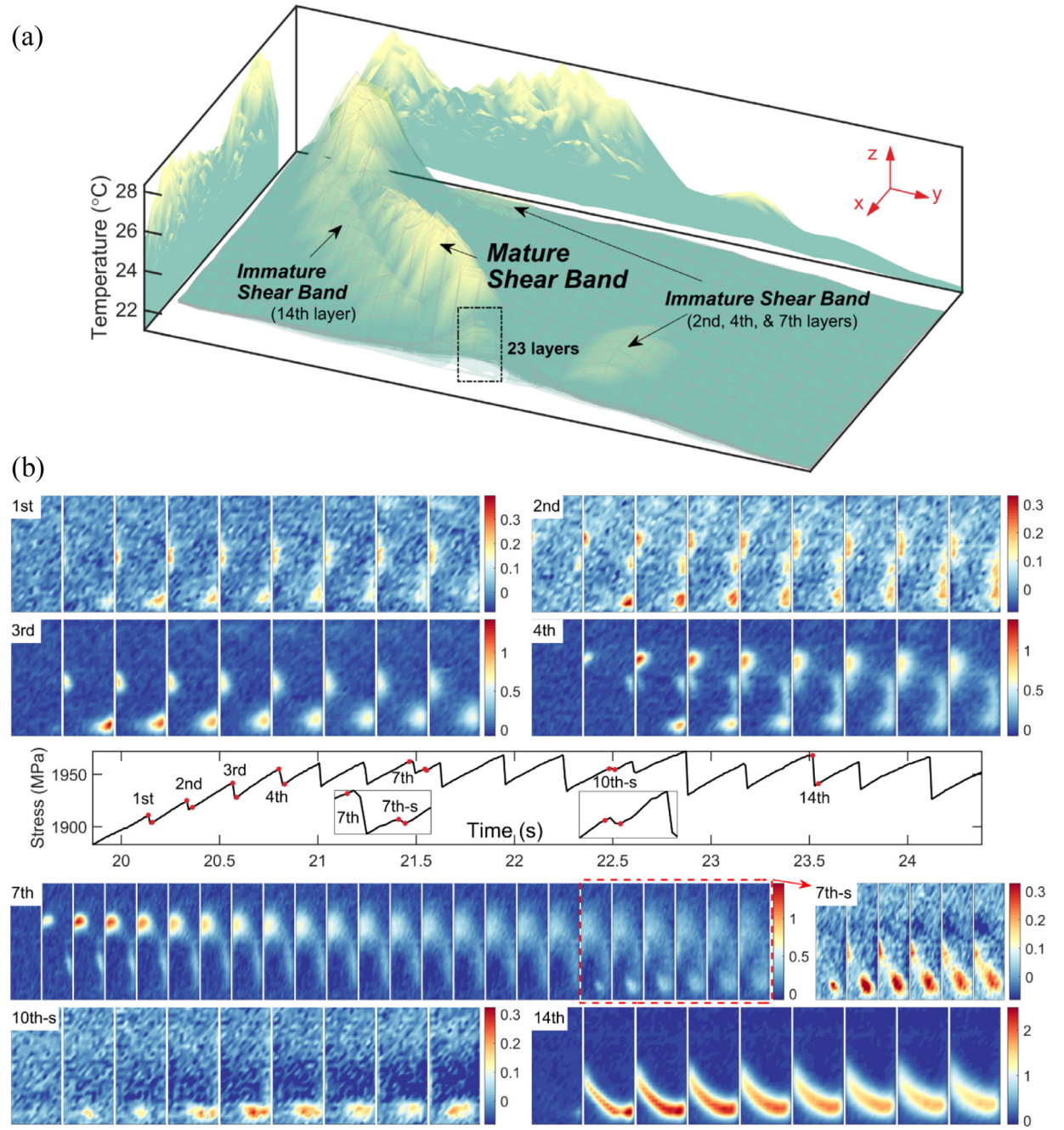

Fig. 2. (a) Ridge-like morphology of the temperature distribution obtained by superimposing the first frame of each serration event (27 layers in total) with appropriate transparency, indicating the locations of mature and immature shear band. 2D projections are plotted on the x-z and y-z planes. (b) Consecutive frames of thermal image show the heat band evolution for 1st-4th, 7th, and 14th serrations as well as small serrations (7th-s and 10th-s). The images represent the temperature differences, which were obtained by subtracting the temperature distribution of one frame before the first frame shown above, respectively. The magnitude of temperature difference is indicated by the color legend (unit: Kelvin).

For most BMGs, the first small stress drop actually can be found far below the nominal yielding point in the stress-strain curve, and some other small stress drops are observed between two serrations or within one serration in the plastic region. It has been under long debate whether these small stress drops should be attributed to machine noises or the interaction between machine and specimen. The current work evidently demonstrates that these small stress drops are related to the shear localization activities. As detailed in upper panel in Fig. 2(b), before the nominal yielding point (1st–4th serrations here), the small stress drops correspond to the nucleation of a shear band. The heat, if generated, inside the specimen will not be large enough to conduct to the surface, and only heated locations at both ends of the shear

band plane, as constrained by the specimen surface, can be detected by IR camera, which appears as a discontinued heat band. Note that the occurrence of the heat bands for each serration may not be at the same location. For example, the locations of the 2nd and 4th serrations are different from those of the 1st and 3rd serrations [Fig. 2(b)]. The results imply that a competition among different shear band nucleation sites exists before the nominal yielding point, which prepares the potential shear plane for the mature shear band propagation. Furthermore, the tiny stress drop overlapped with other large serrations cannot be neglected since they are also coupled with localized temperature burst. As evidenced by these thermal images, the tiny stress drop indeed suggests an activation of a localized shear band, as illustrated in lower panel in Fig. 2(b) for two tiny stress drops between the 7th and 8th, and the 10th and 11th serrations, respectively. To the best of our knowledge, it is for the first time that the IR camera results clarified the physical meaning of the small stress drops before the nominal yielding point as well as during the serration period, providing an informative vision to understanding the shear band operation in BMGs.

4. Discussion

4.1. Spatiotemporal modeling for heat content

The heat content generated during shear band operation has been an interesting topic for a long period (Ketov and Louzguine-Luzgin, 2013; Lewandowski and Greer, 2006; Zhang et al., 2007; Slaughter et al., 2014). In previous studies, heat content, H, was estimated based on the heat converted from the entire work done by shear with an approximated coefficient (Zhang et al., 2007; Matthews et al., 2008; Qiao et al., 2012; Miracle et al., 2011), or deduced by measuring the width of hot band using the fusible coating method (Lewandowski and Greer, 2006), which utilizes the limited number of shear offsets or shearing layer thickness from the microscopic measurement. It seems not easy to acquire the heat release for each serration in the experiment, due to the difficulties in matching each single serration event with the corresponding microscopy-obtained hot-band width (or shear offset, or thickness of shearing layer). However, H carries the information of the extent to which the sample deformed, and thus, should be treated individually for each serration, which is essential to reveal the evolution of shear band activities, as enlightened by the result in Fig. 1(a) that the maximum temperature and stress drop become larger as the external load increases. Therefore, in the present study, a spatiotemporal modeling procedure is proposed to derive H for each serration event coupled with the thermograph data. By considering the moment when the first frame of heat conduction was captured by the camera, a shift time, t_c, was introduced into the thin-film solution of the one-dimensional (1D) heat diffusion equation:

$$\Delta T = \frac{H}{\rho C_p} \cdot \frac{1}{\sqrt{4\pi\alpha(t+t_c)}} \exp\left(\frac{-x^2}{4\alpha(t+t_c)}\right) \tag{1}$$

where H is the heat content, ρ the density of the material, C_p the specific heat capacity, t the elapsed time from the first frame, t_c the time between the beginning of heat generation and first frame camera captured, x the distance from the shear band center, and α the thermal diffusivity. Note that solutions with a finite thickness for heat diffusion was discussed in recent work (Wang et al., 2016), but for simplicity, we adapted the zero thickness solution here. For the materials investigated in the present study, $C_p = 330\,\mathrm{J/kg{\cdot}K}$ (Yang et al., 2006; Glade et al., 2000), $\rho = 6730\,\mathrm{kg/m^3}$ (Wang, 2012), $\alpha = 3\times10^{-6}\,\mathrm{m^2/s}$ (Zhang et al., 2007; Jiang et al., 2008; Matthews et al., 2008). Thus, one can easily obtain the function, $\Delta T(x, t)$, with undetermined H and t_c, which depicts the distribution of temperature rises over spatial and temporal domains. As shown in Fig. 3(a), the temperature data was collected from a path perpendicular to the heat band marked by the black arrow line. Then a surface fitting based on the globally optimized least square method is used to determine H and t_c. The fitting gives the best result when the minimum of the squares of residuals between experimental and predicted values is achieved, and can be expressed as:

$$LQ = \min \sum_i \left|T_i - \hat{T}_i\right|^2 \tag{2}$$

where T_i is the experimental temperature at each point of the spatiotemporal surface (red cross) in Fig. 3, and $\hat{T}_i$ is the predicted value from Eq. 1, which is presented as the color surface in Fig. 3. $|T_i - \hat{T}_i|^2$ is the square of residuals. Given a set of initial values of parameters (i.e., H and t_c), the minimized LQ can be found with enough iterations by setting a tolerance, which is 10^{-16} in this study. Multiple sets of initial values (3000 sets in this study) were used to ensure that the fitting results are globally optimized (details in the supplementary document). Then the fitting was repeated for multiple lines marked by dashed lines in Fig. 3(a) to obtain average values of H and t_c. The results of the fitted H are listed in Table S1. The values range from 789.27 to 8034.31 $\mathrm{J/m^2}$ for Vit-105, which is well comparable to the estimated H of 400 – 2200 $\mathrm{J/m^2}$ for Vit-1 (Lewandowski and Greer, 2006). Moreover, the fitting method readily shows that the amount of heat release follows an increasing trend as the deformation proceeds.

The accumulated energy stored for each serration event was calculated from the stress-stress curves, and compared to the fitted H. The results were plotted in Fig. 3(c) and listed in Table S1. The average conversion rate of the stored energy to the heat is thus obtained as 0.71 ± 0.17, rather than the constant coefficient, 0.9, which is commonly used as the estimation in the previous work (Qiao et al., 2012; Dalla Torre *et al.*, 2008). This result provides a reference value for future studies.

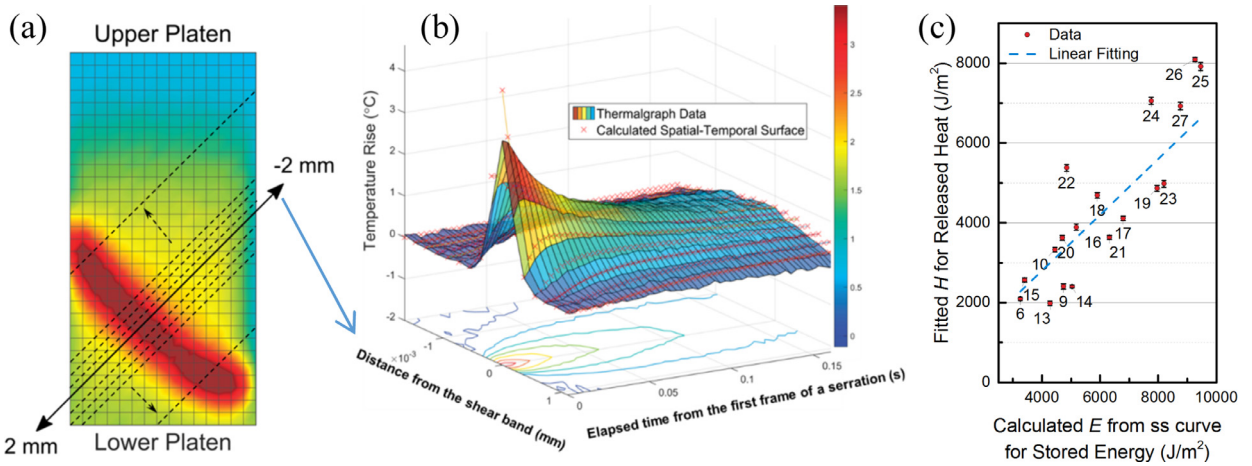

Fig. 3. (a) The linear profile of temperature values used for the spatial calculation, which is perpendicular to the heat band, and multiple lines (dashed) are used to achieve average values. (b) Spatial-temporal surface modeling of the temperature data from thermograph. (c) The relationship between the released heat H obtained from the spatial-temporal surface and the stored energy E calculated from the stress-strain (ss) curve. The marked numbers indicate the sequence of serration events.

4.2. Model of shear band propagation

To ascertain the mechanism behind the serration behavior, a coarse-grained approach based on the shear-transformation-zone (STZ) dynamics was used to assess the local heating effect on the serration behavior in the uniaxial loading (Bulatov and Argon, 1994; Zhao et al., 2013) (see details in the supplementary file). This type of model was first proposed by Bulatov and Argon (Bulatov and Argon, 1994) and later was extended by Zhao *et al.* (Zhao et al., 2013) and Homer *et al.* (Homer and Schuh, 2009). These models have the same spirit that the transformations of an STZ are a state-to-state kinetic event controlled by a kMC algorithm. Correspondingly, the free energy ΔQ of STZ activity is based on Argon's model that is $\Delta Q = \Delta F - \Delta W$, where ΔF is the change of the Helmholtz free energy and ΔW is the deformation work done by the applied stress imposed on the STZ element (Argon, 1979). The rate of STZ transformation relying on the framework of transition-state theory is given by $k_i = v_0 \exp(-\frac{\Delta Q_i}{k_B T})$, where i indicates the i-th STZ element in the system, k_B is Boltzmann's constant, T is the absolute temperature, and v_0 is the trial frequency on the same order of magnitude as Debye frequency. Evidently, the probabilities of STZ transformations depend on the competition between the role of thermal fluctuations and the required amount of ΔQ. It follows that the activation of a STZ gives rise to a redistribution of stress within the system, which may in turn influence the rate of activation of the STZs. Consequently, this kind of model can capture the physics associated with fundamental events of STZs for the process of the nucleation and the propagation of a shear band. Of particular note is that our approach works in the framework of Zhao *et al.* (Zhao et al., 2013), which emphasizes the softening effect through introducing a generation-dependent softening factor to reflect the change of internal structure during a shear band formation. This ad hoc assumption is not needed, since we believe that the shear band evolution can be critically influenced by the thermal softening via the heterogeneity of the heating source distribution. Later discussions will support this line of argument, so that we have integrated the heat diffusion equation in our modified kMC model to make thermal fluctuations behave more realistic as that in experiment. As expected, the simulation shows very interesting results. The stress drops and the temperature bursts are synchronized with each other, as presented in Figure S4, which is consistent with the observation of IR camera in Fig. 1(a).

The softening behavior in metallic glasses can now be attributed to two parts, i.e., structural softening and thermal softening. It has been less controversial that the structural softening drives shear deformation in metallic glasses, but still argued that how an important role the thermal softening plays on the intermittent shear bands, or serration behavior. In other words, why a shear band stops and can be reactivated? We can explain these questions through the physics captured in our modified kMC model and simulations. In a stationary situation of thermal fluctuation, the rate of STZ activities is only determined by $\Delta Q = \Delta F - \Delta W$, and ΔQ will be tilted via ΔW as the applied stress increases. Until thermal fluctuations can compete with this amount ofΔQ, the incidence of STZs will rise. This is the early stage of structural softening and always arises at the yielding or in the beginning of each serration. Soon after that, the local heat generates because of the released plastic work and may cause apparently local temperature increase. This local temperature increment amplifies thermal fluctuations and further facilitates the activity of STZs. This is a superposition of the thermal softening and the structural softening. Heat conduction makes this effect spread out to their surroundings to trigger a chain of reactions of STZs, like avalanche, which results in a sudden drop in the stress-strain behavior. At late stages of this process, due to the stress reduction, the activation energy barriers of STZs are reinstated, and due to the heat dissipation, the local temperature increment becomes small. Thus, both factors lower the incidence of STZs. As a result, the shear band stops. Nevertheless,

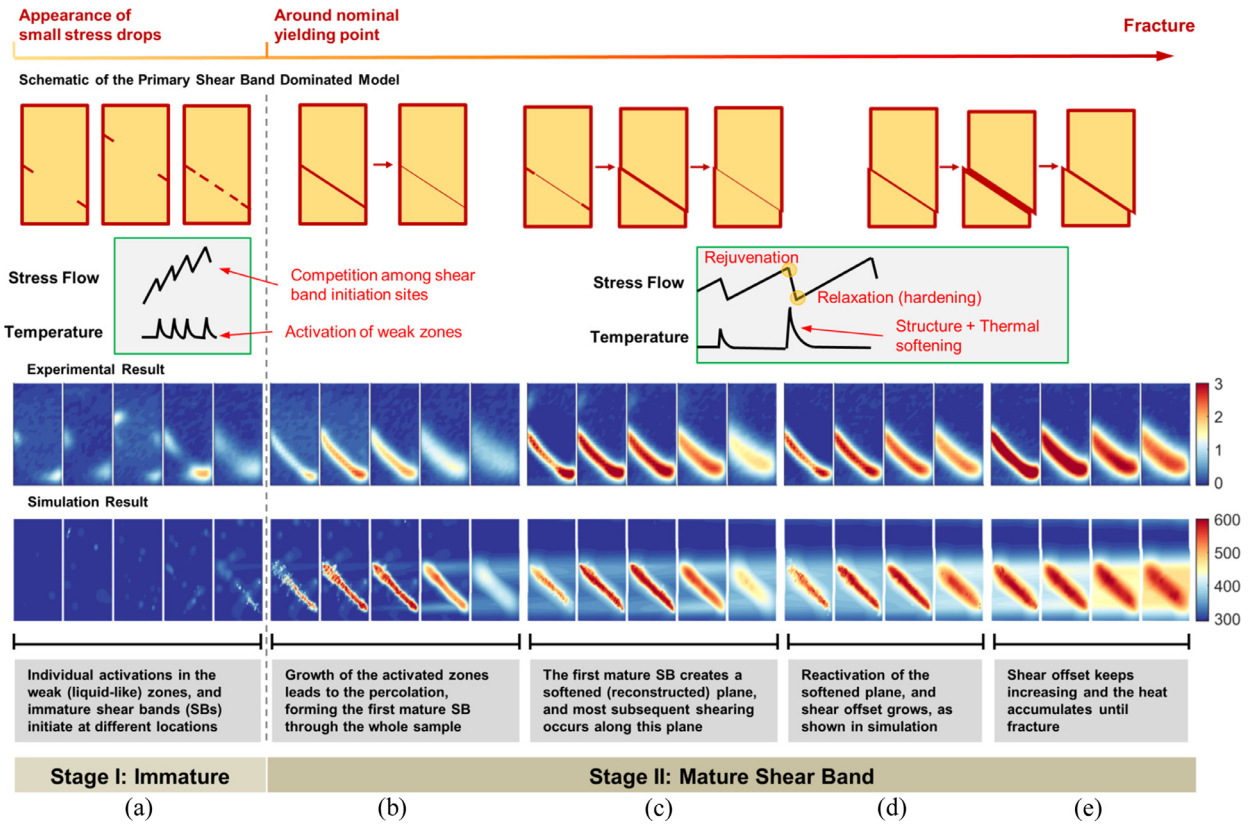

Fig. 4. The deformation modes in different periods from pre-yielding to fracture. The top arrow line shows the key points in the stress-strain curve, and below it the schematic shows the evolution of the primary shear band dominated model, with magnified stress flow and temperatures showing shape features at different stages. The lower panel shows the comparison of IR experimental and kMC simulation results with interpretations (color bar unit: Kelvin). The simulation result is from our small size model with scaled thermal diffusivity at nano size. The difference of temperature range between experimental and simulation is due to the different observing areas and time windows. The real-size kMC model with real thermal diffusivity can be found in Figures S4-S6 (supplementary document). The bottom part shows the two-stage partition.

the shear banding leaves more free volume in the shear-band plane than its vicinity, which is known as one of the key features of the generation-dependent softening model (Zhao et al., 2013). Hence, at next cycle the opportunity for shear band initiation at this plane again will be much higher than the other planes. The above mechanism had been proved in our simulations and agrees with our experiments. This thermal disturbance on the flow stress spontaneously induces the periodicity of serrations until the fracture of the sample or changes of the loading condition.

Through a further examination and comparison of more serrations in thermal images and simulations, an excellent agreement can be found between them, as illustrated in Fig. 4. It suggests that the deformation can be divided into two stages: immature and mature shear band stages, which are termed as Stages I and II for simplicity. Combined with the recent progress in the understanding of the local deformation in BMGs, the model of shear band evolution is elaborated as follows. It has been reported that BMGs are composed of solid-like and liquid-like (or anelastic, weak) regions (Li et al., 2013; Egami, 2011; Dmowski et al., 2010; Liu and Yang, 2012; Ye et al., 2010). The liquid-like regions were found to possess a large volume fraction and contribute to structural rejuvenation under external loading (Dmowski et al., 2010; Tong et al., 2015), which are considered to be closely associated with shear band nucleation and serve as the basic deformation units. At Stage I (serrations 1-4), a shear band plane is formed as a potential sliding path, and the heat generated at the top and bottom ends of shear band plane (illustrated in Figure S1) can be observed by IR camera, indicating a non-uniform heat generation (or weak-zone activation) inside the shear band plane. Meanwhile, the simulation results of Fig. 4(a) show the individual activations (spots in light color) of weak zones, corroborating the heterogeneous heat generation in above experimental observation. Competition may exist in different places for shear band nucleation, which can be evidenced by the different locations of bright spots in both experimental and simulation figures. All the findings suggest that the assumption of the planar heating source to calculate the heat conduction fails at Stage I. Within Stage II (serrations 5-27), the activated weak zones “percolates” from both ends of the shear band plane, with more and more heat generated, and a continued heat band forms [Fig. 4(b)]. From now on, the deformation is mainly accommodated within this shear band plane (heat percolated or softened path) [Fig. 4(c)], as demonstrated in Figure S2. As discussed above in the last paragraph of Results section, a few localized shear band activations lead to the tiny stress drop, which overlaps the large stress drop. The

released heat becomes larger as the external load increases, which may be attributed to the continuously weakened path by repeated serration events, as well as the shear offset along the softened path [Fig. 4(d, e)]. Note that the IR camera actually captured the heat conduction process of the shear band reactivation (e.g., 8th and 11th serrations in Figure S2), which shows one or two frames with a lighter band before hottest band appears. This long conduction (millisecond) indicates that shear band is reactivated inhomogeneously, hot at core, but cold at the edge (sample surface), which interprets why shear band is not always hot, as argued in recent fusible coating works from the fact that no tin melted before fracture[12, 22]. The above two-stage model can be referred as primary shear band dominated model, and is especially suitable for relatively brittle BMGs. There are actually other cases where multiple shear bands dominate for relatively ductile BMGs, which is a more complicated process involving shear band interaction. The results revealed by IR camera are indispensable to obtain the whole picture of the shear band evolution process.

5. Conclusion

For the first time, our modified kMC model simulated the successive occurrence of serration behavior, which demonstrated the importance of local heating effects. A spatiotemporal surface fitting method was developed to estimate the released heat content for each individual serration, and the results are well comparable to those obtained by the other experimental methods. Through the correlation with thermal imaging results, the present work clarified the following issues for BMGs which has not been well understood or been neglected: (1) one to one correspondence between the stress drop and shear band activities, (2) small stress drops before yielding and among large serrations, (3) reactivation (or simultaneous “propagation”) of primary shear bands in one softened plane, and (4) a linear relationship between the stress drop and temperature rise for each serration. Furthermore, a primary shear band dominated model was proposed to describe the deformation behavior of most relatively brittle BMGs. The present work is expected to advance the understanding for the shear band activities, and encourage the development of relevant theories and models for BMGs or other amorphous materials.

Acknowledgements

XX and PKL very much appreciate the financial support from the US National Science Foundation (DMR-0909037, CMMI-0900271, CMMI-1100080, and DMR-1611180), the Department of Energy (DOE), Office of Nuclear Energy’s Nuclear Energy University Program (NEUP) 00119262, the DOE, Office of Fossil Energy, with National Energy Technology Laboratory (DE-FE-0008855), and the U.S. Army Research Office (W911NF-13-1-0438), with Drs. Huber, Cooper, Finotello, Ardell, Taleff, Cedro, Jensen, Tan, Lesica, Farkas, Bahas, and Stepp as contract monitors. YCL and SO acknowledge support by ESISM Japan. YCL appreciates the support from MOST 105-2218-E-009-026. SO acknowledges support by JSPS KAKENHI (Grant Nos. 22102003, 23246025, and 25630013). KAD gratefully acknowledges the NSF grants of DMR-1005209 and DMS-1069224. KAD and PKL are grateful to the DOE, Office of Fossil Energy (DE-FE-0011194) with Dr. Mullen as contract monitor. HQ and YG acknowledge a seed grant from the Office of Research and Engagement, the University of Tennessee.

Supplementary materials

Supplementary material associated with this article can be found, in the online version, at doi:10.1016/j.jmps.2018.11.015.

References

Argon, A.S., 1979. Acta Metallurgica 27, 47.
Ashby, M.F., Greer, A.L., 2006. Scripta Materialia 54, 321.
Bulatov, V.V., Argon, A.S., 1994. Modelling and Simulation in Materials Science and Engineering 2, 167.
Cao, A.J., Cheng, Y.Q., Ma, E., 2009. Acta Materialia 57, 5146.
Dalla Torre, F.H., Dubach, A., Schällibaum, J., Löffler, J.F., 2008. Acta Mater 56, 4635.
Dmowski, W., Iwashita, T., Chuang, C.P., Almer, J., Egami, T., 2010. Physical Review Letters 105.
Egami, T., Iwashita, T., Dmowski, W., 2013. Metals 3, 77.
Egami, T., 2011. Progress in Materials Science 56, 637.
Gao, Y.F., Yang, B., Nieh, T.G., 2007. Acta Materialia 55, 2319.
Glade, S.C., Busch, R., Lee, D.S., Johnson, W.L., Wunderlich, R.K., Fecht, H.J., 2000. J. Appl. Phys. 87, 7242.
Greer, A.L., Cheng, Y.Q., Ma, E., 2013. Mater. Sci. Eng., R 74, 71.
Greer, A.L., 1995. Science 267, 1947.
Homer, E.R., Schuh, C.A., 2009. Acta Materialia 57, 2823.
Jiang, W.H., Liao, H.H., Liu, F.X., Choo, H., Liaw, P.K., 2008. Metallurgical and Materials Transactions a-Physical Metallurgy and Materials Science 39A, 1822.
Johnson, W.L., 1999. Mrs Bulletin 24, 42.
Ketov, S.V., Louzguine-Luzgin, D.V., 2013. Sci. Rep. 3.
Klaumunzer, D., Maass, R., Loffler, J.F., 2011. J. Mater. Res. 26, 1453.
Klaumunzer, D., Lazarev, A., Maass, R., Torre, F.H.D., Vinogradov, A., Loffler, J.F., 2011. Phys. Rev. Lett. 107.
Kumar, G., Desai, A., Schroers, J., 2011. Adv. Mater. 23, 461.
Leamy, H., Wang, T., Chen, H., 1972. Metall and Materi Trans B 3, 699.
Lewandowski, J.J., Greer, A.L., 2006. Nature Mater 5, 15.
Li, W.D., Bei, H., Tong, Y., Dmowski, W., Gao, Y.F., 2013. Appl. Phys. Lett. 103, 5.
Liu, Z.Y., Yang, Y., 2012. Intermetallics 26, 86.
Matthews, D.T.A., Ocelik, V., Bronsveld, P.M., De Hosson, J.T.M., 2008. Acta Materialia 56, 1762.

Miracle, D.B., Concustell, A., Zhang, Y., Yavari, A.R., Greer, A.L., 2011. Acta Materialia 59, 2831.
Qiao, J.W., Jia, H.L., Zhang, Y., Liaw, P.K., Li, L.F., 2012. Mater. Chem. Phys. 136, 75.
Slaughter, S.K., Kertis, F., Deda, E., Gu, X., Wright, W.J., Hufnagel, T.C., 2014. Apl Materials 2.
Song, S.X., Nieh, T.G., 2011. Intermetallics 19, 1968.
Thurnheer, P., Haag, F., Löffler, J.F., 2016. Acta Mater 115, 468.
Tian, L., Cheng, Y.-Q., Shan, Z.-W., Li, J., Wang, C.-C., Han, X.-D., Sun, J., Ma, E., 2012. Nat Commun 3, 609.
Tong, Y., Iwashita, T., Dmowski, W., Bei, H., Yokoyama, Y., Egami, T., 2015. Acta Materialia 86, 240.
Wang, W.H., Dong, C., Shek, C.H., 2004. Mater. Sci. Eng., R 44, 45.
Wang, C.C., Ding, J., Cheng, Y.Q., Wan, J.C., Tian, L., Sun, J., Shan, Z.W., Li, J., Ma, E., 2012. Acta Mater 60, 5370.
Wang, G.Y., Feng, Q.M., Yang, B., Jiang, W.H., Liaw, P.K., Liu, C.T., 2012. Intermetallics 30, 1.
Wang, J.G., Pan, Y., Song, S.X., Sun, B.A., Wang, G., Zhai, Q.J., Chan, K.C., Wang, W.H., 2016. Materials Science and Engineering: A 651, 321.
Wang, W.H., 2012. Prog. Mater. Sci. 57, 487.
Wright, W.J., Schwarz, R.B., Nix, W.D., 2001. Mater. Sci. Eng., A 319, 229.
Wright, W.J., Samale, M.W., Hufnagel, T.C., LeBlanc, M.M., Florando, J.N., 2009. Acta Mater 57, 4639.
Wright, W.J., Byer, R.R., Gu, X.J., 2013. Appl. Phys. Lett. 102, 4.
Yang, B., Liu, C.T., Nieh, T.G., Morrison, M.L., Liaw, P.K., Buchanan, R.A., 2006. Journal of Materials Research 21, 915.
Ye, J.C., Lu, J., Liu, C.T., Wang, Q., Yang, Y., 2010. Nature Materials 9, 619.
Zhang, Y., Stelmashenko, N.A., Barber, Z.H., Wang, W.H., Lewandowski, J.J., Greer, A.L., 2007. J. Mater. Res. 22, 419.
Zhao, P., Li, J., Wang, Y., 2013. International Journal of Plasticity 40, 1.